COBEM 2023 27TH INTERNATIONAL CONGRESS OF MECHANICAL ENGENEERING

ABCM Brazilian Society of Mechanical Sciences and Engineering
27th ABCM International Congress of Mechanical Engineering
December 04-08, 2023, Florianópolis-SC, Brazil

COB-2023-1076
ANALYSIS OF THE EFFECT OF PERTURBATIONS IMPOSED ON THE SUPERSONIC FLOW OVER A CYLINDER THROUGH DIRECT NUMERICAL SIMULATIONS

Allan Rodrigo Souza
Leonardo Santos de Brito Alves
Juan Carlos Assis Silva
Universidade Federal Fluminense, Rua Passo da Pátria, 156 - Niterói - Rio de Janeiro, Brazil
souzaallan@id.uff.br, lsbalves@id.uff.br, jcasilva@id.uff.br
Rômulo Bessi Freitas
Centro Federal de Educação Tecnológica Celso Suckow da Fonseca, Estrada de Adrianópolis, 1.317, Santa Rita, Nova Iguaçu - RJ, Brazil
romulo.freitas@cefet-rj.br

Abstract. *The supersonic flow around a two-dimensional cylinder has been studied for many decades using direct numerical simulations to determine accurate steady-states. Linear and global stability analyses of these steady-states show the flow is modally stable, i.e. the time asymptotic behavior of small amplitude two-dimensional disturbances shows an exponential decay in time. On the other hand, a significant optimal non-modal disturbance energy growth has been recently observed at the shock. The present study aims disturb the shock in order to verify the realizability of the non-modal energy growth. This is done by rotating the cylinder wall in different ways after the flow has reached steady-state, which allows these disturbances to propagate upstream within the subsonic region between solid wall and shock and interact with the shock. Preliminary results indicate doing so changes the shock location but induces no sub-optimal energy growth.*

Keywords: *Aerodynamic Disturbances, Supersonic Flows, Direct Numerical Simulation, DNS*

1. INTRODUCTION

The study of supersonic flows around a cylinder holds significant relevance across many fields of knowledge, including aerospace engineering, defense, and security. Moreover, understanding and controlling the flow around aerodynamic objects are crucial for advancing air travel technologies and enabling the expansion of its applicability to other sectors (Anderson, 2023). A recent investigation using direct numerical simulations (DNS) and linear stability analyses (LSA) identified the presence of a non-modal transient growth of the perturbations in the supersonic flow in front of a cylinder by an order of 10^3 magnitudes (Alves, 2021). This was observed, however, under optimal initial conditions. Hence, the realizability of sub-optimal initial condition is still unknown.

DNS is used here as a method to complement the LSA and enable a detailed evaluation under different excitation conditions to investigate the sub-optimal non-modal behavior. These simulations solve the equations of mass, momentum, and energy balance that govern fluid behavior at multiple points in space and time. They allow the capture of important flow details, such as boundary-layers and shock waves. Although they require substantial computational resources, they provide numerical solutions with high-resolution in space and time, which is a crucial element for validating such non-modal instabilities that lead to transient growth and for providing precise insights into the flow dynamics across various perturbation regimes (Hirsch, 2007).

This study is performed for the same supersonic flow upstream of a rigid cylinder investigated originally (Alves, 2021). Specifically, tangential and normal oscillatory pulses are introduced at the cylinder wall during steady-state conditions to assess their effects on the flow and bow shock. In this approach, the wall velocity components are manipulated to emulate cylinder oscillations while maintaining boundary conditions for impermeability, adiabatic wall, zero wall-normal velocity and no-slip at the cylinder wall. The solution was monitored suing the both velocity components, Mach number, pressure, specific mass and temperature of the flow in the entire simulated domain.

2. METHODOLOGY

The adimensional number that carries the relationship between the flow and the limit velocity of pressure waves in a fluid (the sound speed a_o) is the Mach number (M). In general, problems involving external flow around blunt and cylindrical bodies are often simplified by considering air as an incompressible fluid. However, this assumption becomes invalid for isothermal flows with $M_\infty > 0.3$, and regions of discontinuity in the properties could appear, known as shock

waves. These are stationary pressure waves that mark the boundary beyond which information from the body within the flow cannot travel upstream (Anderson, 2020). Due to their arc-shaped profile, they are also referred to as bow shocks. As shown in Fig. 1.a and b, the bow shock for a low supersonic flow is less concave than the one in a hypersonic flow.

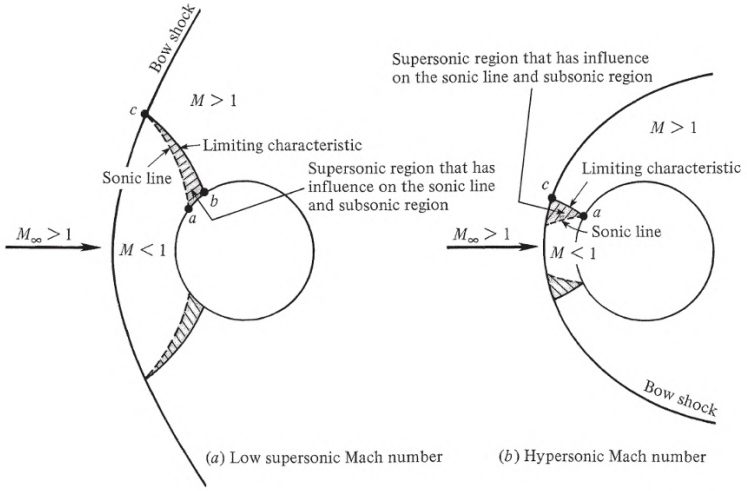

Figure 1. Shock wave shape for supersonic and hypersonic flow adapted from Anderson (2020).

2.1 Simulation domain

The DNS code used to perform the simulations for this work was implemented using C++ with the package PETsC (Abhyankar *et al.*, 2018), which is also used for advancing the solution in time. This code uses the fifth-order WENO scheme for spatial discretization of inviscid fluxes and central difference schemes for viscous fluxes. The mesh used here is generated with an in-house code (Nunes, 2021).

Additionally, the boundary conditions are incorporated into the code through the relevant mesh points. The two-dimensional simulation of the unitary cylinder was conducted within the unitary computational domain $[\xi, \eta]$, which was then mapped to the physical elliptic space $[x, y]$. When using an analytic mesh for the front portion of this cylinder, Equations 1 (Jiang and Shu, 1996) are employed.

$$\begin{cases} x(\xi,\eta) = (R_x - (R_x - \kappa)\xi)\cos(\theta\,(2\eta - 1)) \\ y(\xi,\eta) = (R_y - (R_y - \kappa)\xi)\sin(\theta\,(2\eta - 1)) \end{cases} \tag{1}$$

where R_x, R_y, θ, and κ are the left, top, and respectively the bottom boundaries of the domain, angular opening, and right wall (the cylinder's wall). Thus, Santos (2020) presents the parameters $R_x = 1.0$, $R_y = 1.5$, $\theta = 5\pi/12$ and $\kappa = 0.5$ that generate the shaded region bounded by the blue line shown in the Fig. 2.

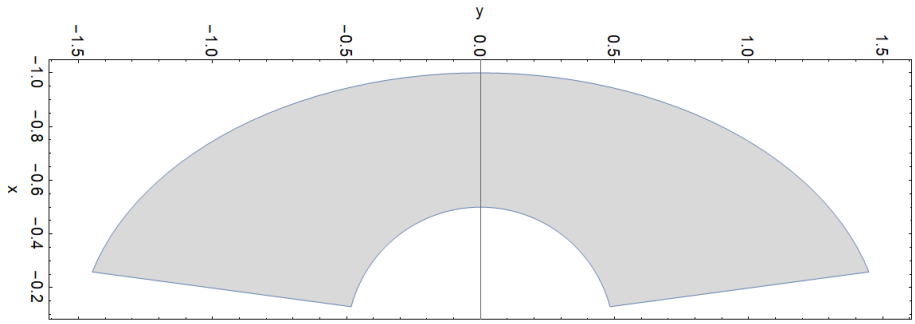

Figure 2. The two-dimensional space of the simulation rotated 90 degrees.

2.2 Steady-state

Given the physical discontinuity present in this problem, the technique described in Santos and Alves (2019) was employed to generate a steady-state solution that accurately captures the presence of the shock wave, for the atmospheric air with $\gamma = 1.4$, $Pr = 0.72$, $M_\infty = 6$ and $Re = 10^3$. The properties at the inlet boundary were set as $P_\infty = 67.01$

Pa, $T_\infty = 271.15\ K$, $v_\infty = 0\ m/s$ and $u_\infty = 1980.64\ m/s$, which remained constant throughout the simulation. The computational domain was discretized with a mesh consisting of [201,401] points homogeneously distributed. Figure 3 shows the converged output for the steady state of the simulation which confirms the shock wave presence.

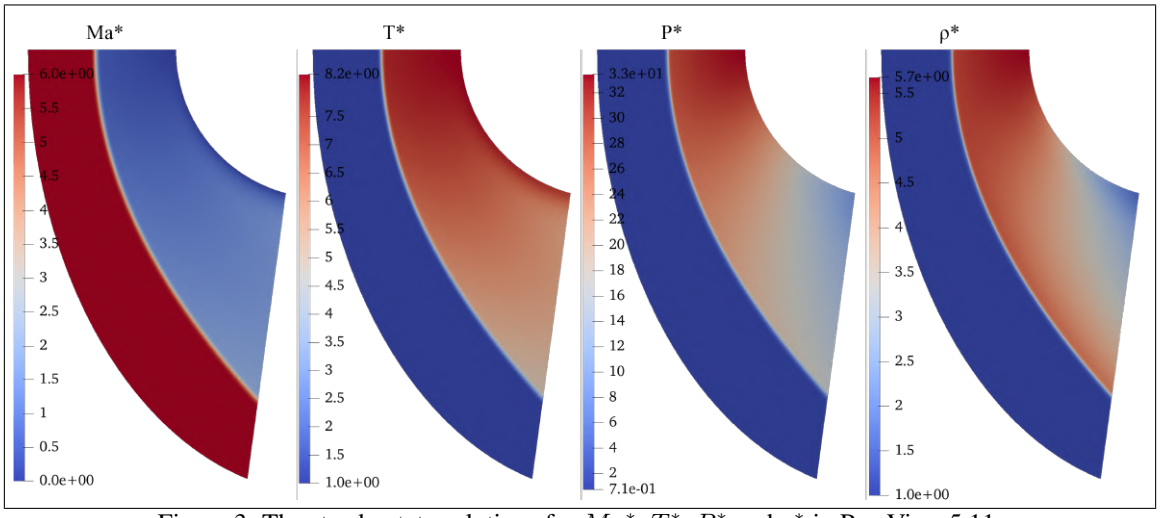

Figure 3. The steady-state solutions for Ma^*, T^*, P^* and ρ^* in ParaView 5.11.

By performing data processing, it is possible to validate comparatively the solutions with the one presented by Anderson in Fig. 4. As shown in Fig. 1, the sonic line refracted as the limit of the red area can also be observed, exhibiting a similar shape to that shown in Fig. 4. The difference is that in the simulation conducted here, the viscous effects of the problem were taken into account using Sutherland law with $C_1 = 1.458\ 10^{-6}\ kg\ m^{-1}\ s^{-1}\ K^{-1/2}$ and $S = 110.4K$. This difference will be reflected in the increase of the subsonic region, both by moving away from the wall and by becoming wider, and in the appearance of a boundary layer on the surface of the cylinder. This phenomenon can be tested by increasing the Reynolds number input in the simulation. However, that is not the focus of this work.

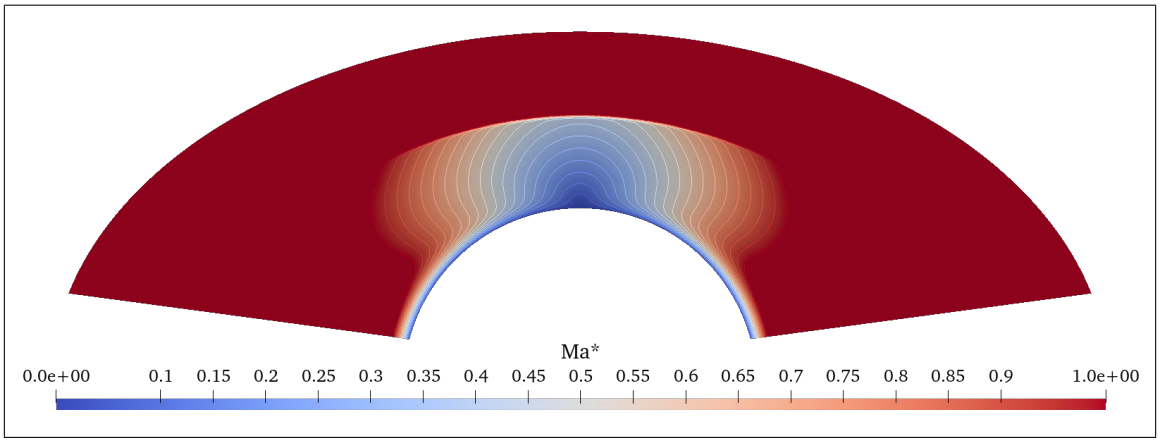

Figure 4. Render of the data analysis isolating the subsonic region.

2.3 Estimates the shock position

The shock wave is a fluid-dynamic phenomenon that occurs when an object moves at a speed greater than the speed of sound in the medium in which it is immersed. The fundamental relationship between shock waves and pressure changes justifies the choice of pressure as a key parameter because a shock wave is characterized by a rapid increase in pressure followed by a sudden decrease, resulting in a discontinuity in the flow properties (Anderson, 2020).

The bow shock observed in the Fig. 3 has a parabolic shape, and since the simulation domain in physical space exhibits symmetry with the x-axis, the Eq. (2) is sufficient to describe the shock,

$$x[y] = \alpha\, y^2 + x[\xi_{CS}, \eta_C] \qquad \alpha = \frac{x[\xi_{BS}, \eta_B] - x[\xi_{CS}, \eta_C]}{(y[\xi_{BS}, \eta_B])^2} \tag{2}$$

where β is the called concavity constant, ξ_{CS} is the found value of bow shock in the middle of computational space, $\eta_C = 0.5$. The domain of Eq. (2) is delimited for $y[\xi_{BS}, 0] \leq y \leq y[\xi_{BS}, 1]$, in which ξ_{BS} is the computational

position of the shock wave at $\eta_B = 0$ or $\eta_B = 1$, a.k.a. the computational position of the shock wave at domains border, these values tend to be equal because the problem is symmetric. It is worth noting that in a computational domain that encompasses the flow downstream of a cylinder, the shock is better fitted by a hyperbolic curve within this range of Mach numbers (Billig, 1967). It is assumed that the shock is located at the point of inflection for $0 \leq \xi \leq 1$ at a fixed η, Since the method of solution employed dampens the shock discontinuity in order to enhance the solver's stability, given the presented conditions. In this way, the shock in the steady state can be quantified by analyzing the data at $\eta = 0.5$ and $\eta = 1$, as shown in Fig. 5.

The data obtained in the steady-state solution of the problem were extracted with two vectors $\eta_{\mathbf{C}}$ and $\eta_{\mathbf{B}}$, stagnation and border line, as shown in the left graph of the Fig. 5 over the simulated domain, which results in two normalized graphs for the pressure behavior along the vectors, Fig. 5.a and Fig. 5.b, respectively. Red lines, translated as red dots over the vectors, in the first graph were obtained by calculating the inflection point of the pressure profiles.

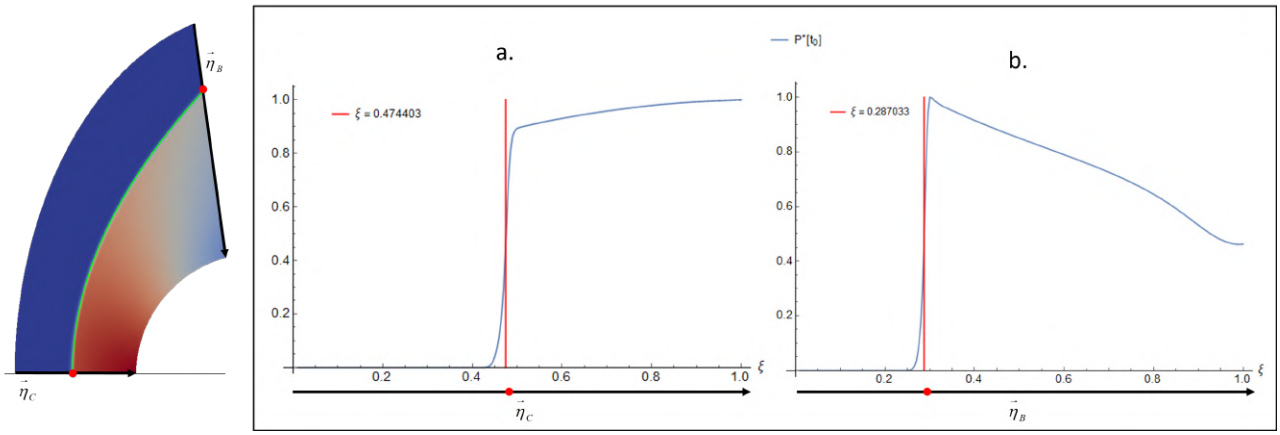

Figure 5. Data Acquisition for Estimating Shock Wave Position: Rendering and Graphical Analysis

Hence, the equation presents the steady-state flow field with a bow shock, depicted in which compares the estimated results and the DNS output. Figure 6.a displays the yellow curve over the generated domain, as shown in Fig. 2. On the other hand, Fig. 6.b presents the green dotted curve applied to the simulation results for the pressure field at the steady state of the problem as seen in Fig. 3, which fits satisfactorily in the shock wave area.

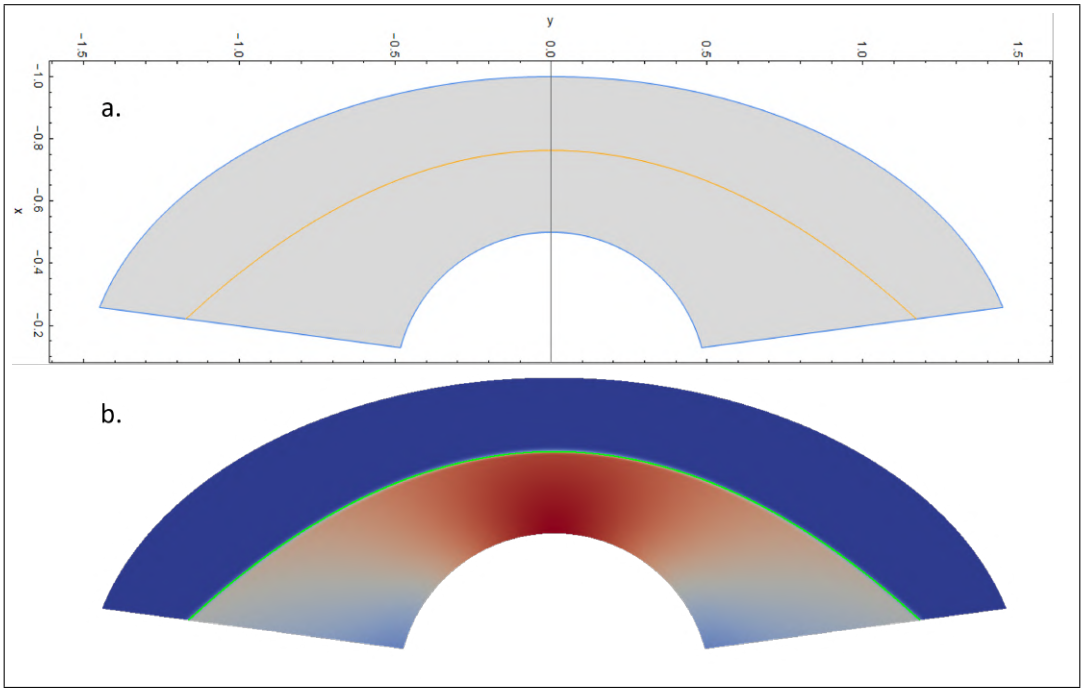

Figure 6. Visual analysis of the Shock estimated 90 degrees. (a) Analytical Graphic; (b) rendered solution.

2.4 Introduction of disturbances on the cylinder wall.

Several disturbances can be stimulated in this supersonic cylinder problem. This is done here with the goal of assessing their effects on the flow, particularly their interaction with the originally steady shock over time. In order to do so, it is necessary to decompose the normal ϵ_N and tangential ϵ_T perturbations on the cylinder wall into their respective x and y components due to the characteristics of the code, which receives the latter as input for the velocity boundary conditions. By decomposing these perturbations, as shown in Fig. 7, we can simulate different velocity inputs at the cylinder wall in order to study their effects on the flow field, including their interactions with the shock wave.

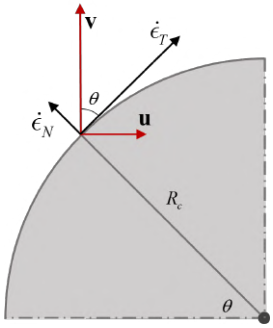

Figure 7. Vectorial decomposition of perturbations into $\mathbf{u}$ and $\mathbf{v}$ components.

The vector decomposition presented in the Eq. (3) expresses the normal and tangential perturbations in terms of the inputs u and v, to be inserted in the code as scalar quantities without losing its essence. These equations provide a formal framework for analyzing the spatial distribution of the perturbations. Furthermore, the normal perturbation, denoted as ϵ_N, represents the component of the velocity field that is perpendicular to the surface, whereas the tangential perturbation, denoted as ϵ_T, represents the component of the velocity that is parallel to the surface.

$$\begin{cases} \mathbf{u}_\epsilon = \dot{\epsilon}_T \sin\left[\tan^{-1}\left(\frac{y[\xi,\eta]}{x[\xi,\eta]}\right)\right]\hat{\theta} + \dot{\epsilon}_N \cos\left[\tan^{-1}\left(\frac{y[\xi,\eta]}{x[\xi,\eta]}\right)\right]\hat{\mathbf{r}} \\ \mathbf{v}_\epsilon = -\dot{\epsilon}_T \cos\left[\tan^{-1}\left(\frac{y[\xi,\eta]}{x[\xi,\eta]}\right)\right]\hat{\theta} + \dot{\epsilon}_N \sin\left[\tan^{-1}\left(\frac{y[\xi,\eta]}{x[\xi,\eta]}\right)\right]\hat{\mathbf{r}} \end{cases} \tag{3}$$

It is noted that equations Eq. (3) are expressed as a linear combination of the unit vectors in the tangential $\hat{\theta}$ and radial $\hat{\mathbf{r}}$ directions with respect to the velocity of the flow in x ($\mathbf{u}_\epsilon$) and y ($\mathbf{v}_\epsilon$) directions. Therefore, to introduce only rotation, the tangential part of these vectors must be equal to 0, while for blowing and suction, the component in the θ direction must be zero. Since the objective is to introduce perturbations on the cylinder wall, it is sufficient to set $\xi = 1$ and maintain the range of η. For the case of a rotational perturbation, a transformation was performed to introduce it in angular form, in degrees, which is shown in Eq. (4).

$$\dot{\epsilon}_T = \dot{\theta}_p \frac{\pi R_c}{180} \qquad\qquad \dot{\epsilon}_N = \dot{\theta}_p \tag{4}$$

A pulse is defined as an oscillatory disturbance with only one wave sign. Among the many existing equations that define a wave, equations derived from the traditional Gaussian equation, with phase shift have been introduced below

$$\theta_p(t) = e^{-\omega^2(t-\beta)^2} \qquad \beta = t_0 + \frac{T}{2} \qquad \omega = \frac{2\pi}{T} \tag{5}$$

where β represents the phase adjustment ensuring that t_0 corresponds to the starting instant, ω stands for the frequency of oscillation, and T represents the period of the disturbance, expressed in dimensionless time units (t_u).

Therefore, to simulate this pulse, it is necessary to incorporate it into the boundary condition of the problem and include a factor corresponding to the amplitude of the disturbance, defined here as θ_{max}. This base equation selected for the purpose of this article was carefully chosen to mitigate the potential disruptions introduced by simulated discontinuities, ensuring the stability of the DNS methods used. This equation is used to apply an oscillatory pulse in the tangential direction in which its derivative follows the chosen equation and can be applied to equation either Eq. (6) or Eq. (7), to stimulate the excitation shown in either Fig. 8 or Fig. 9, respetively. Their phase parameters are set as $T = 0.1\ t_u$, $t_0 = 0.0\ t_u$, and $\theta_{max} = 1.0°$.

$$\theta_{\text{uni}}(t) = \theta_{\text{max}}\ \theta_p(t) \tag{6}$$

$$\theta_{bi}(t) = \theta_{\text{max}}\ \dot{\theta}_p(t)/2 = -\theta_{\text{max}}\ \theta_p(t)\ \omega^2(t-\beta) \tag{7}$$

It is important to observe that Fig. 8 illustrates the introduction of a unidirectional pulse. In this case, during the pulse, the cylinder will smoothly initiate a positive rotation of 1 degree and then return smoothly to its initial position. On the other hand, in Fig. 9, the cylinder will undergo the same positive rotation of 1 degree, but it will return and continue in the opposite direction until it reaches -1 degree from the initial position. Only then it will return to the initial position.

Both, Figure 8 and 9, show the correspondent pulse in black and its corresponding time derivative in red and the points indicated in orange, the initiation and termination of the pulse.

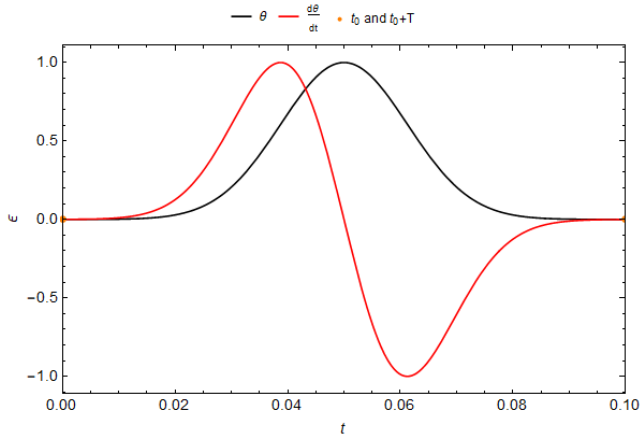

Figure 8. Unidirectional Gaussian disturbance.

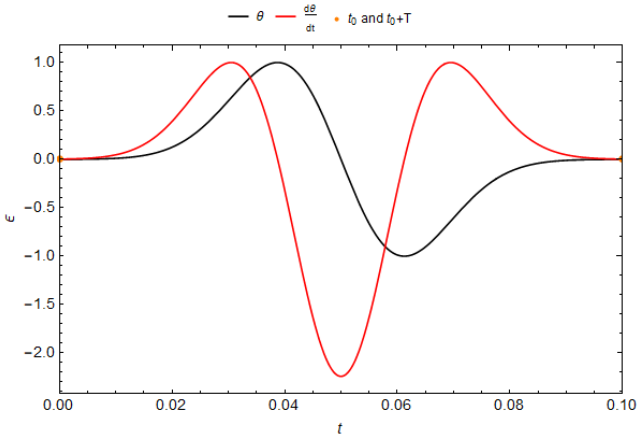

Figure 9. Bidirectional Gaussian disturbance.

Naturally, these disturbances forced at the cylinder wall will eventually become a pressure wave that carries phase and energy information without any mass transference. The flow will act as a restoring force and the resulting pulse will travel upstream mirroring an elastic solid with the cylinder's shape (Kundu and Cohen, 2004).

Figure 10 shows a graphic where $\epsilon(t_0)$ and $\epsilon(t_1)$ represent the disturbance at the initial time and when it first reaches the bow shock. The convected wave would go through the bow shock position after t_1, but no disturbance information can pass a stationary shock wave. This work will use DNS highlight this issue for imposed disturbances with any amplitude and frequency.

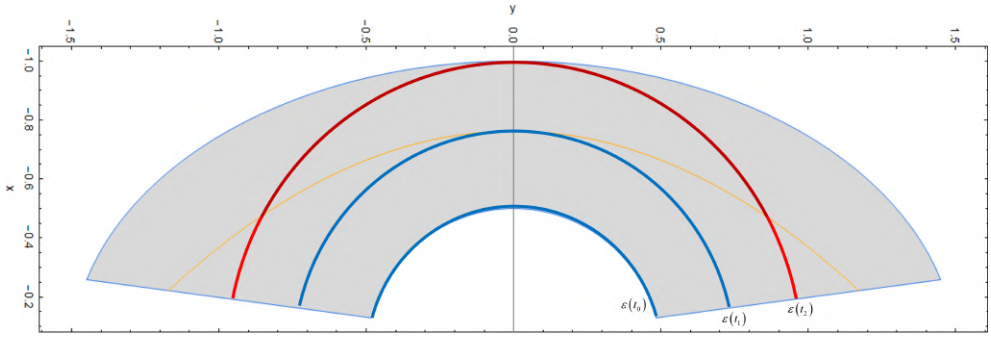

Figure 10. Graphic with the propagation of pressure wave induced.

3. RESULTS

3.1 SHOCK INTERACTIONS

In the interaction analysis between disturbances imposed on the wall of a unitary cylinder and the stationary shock-wave, it can be observed how disturbance propagates within the viscous medium towards the shock in a similar manner in all simulations conducted. As mentioned, the shockwave is a stable phenomenon that does not allow information to pass downstream. However, the selected parameters for the disturbance were able to interact with the shockwave in a way that deviated it from its stable position.

Figure 11 is the consequence of applying Eq. (5) and Eq. (4) in Eq. (3), and the resultant equation in the boundary condition at the cylinder wall ($\eta = 1$) during the stimuli, $t_0 = .001\ t_u$ and $T = .05\ t_u$. So a rotating bidirectional pulse is defined applying Eq. (7) and setting $\dot{\epsilon}_N = 0$ with amplitude $\theta_{\max} = -5°$. The waves generated were captured at $t_1 = 0.096\ t_u$ (First contact with the shockwave) and $t_2 = 0.188\ t_u$ (after contact). A white dashed line was delineated to approximate the wavefront and extrapolate its position as it would be if it did not interact with the shockwave. At $\epsilon(t_1)$, we observe the initial contact of this wavefront with the shockwave towards the stagnation point, where some of

the energy begins to be absorbed. At $\epsilon(t_2)$, the wave continues to collide along the domain's exit boundary, and the stationary shockwave takes the form of interference with the one in the steady state (dashed green line), as can be seen in the zoomed-in square in the space where the wave collides and pushes the shockwave away toward the free-stream.

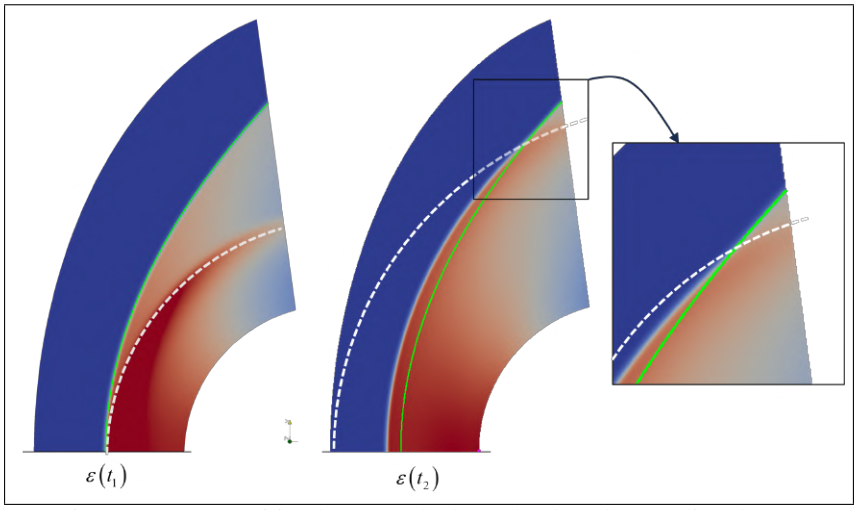

Figure 11. Interposition between the bow shock and wave disturbance

The moment in time when the shockwave is pushed by the wave has been captured in Figure 12. Witch shows the gray-toned lines representing the transition's period with a step of $0.02\ t_u$, the light gray curve spanning from t_1 to t_2, and the red curve representing the pressure profile in the steady-state converged solution. The wave carries a pressure with an amplitude approximately 40% higher than that of the steady-state regime and brings with it a depression with an amplitude of around 10% lower. The wavefront is then damped at the shockwave as it transfers energy to displace it, ultimately reducing pressure along the subsonic zone.

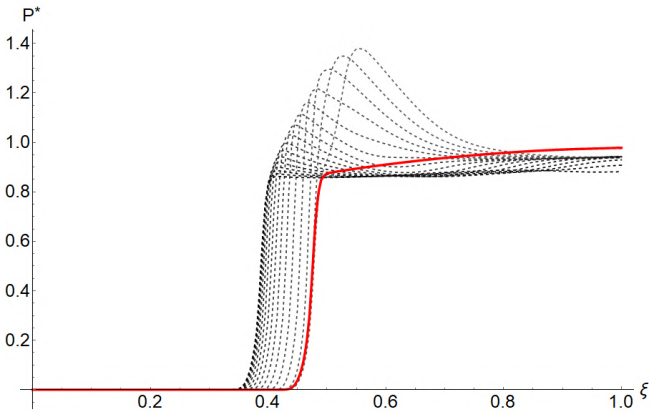

Figure 12. Pressure curve behavior during wave interaction with shock.

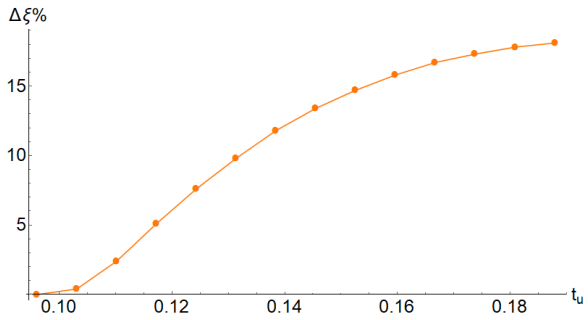

Figure 13. Variation of shock position.

Figure 13 represents the percentage relative deviation from its inertia position during contact. A maximum deviation of approximately 18% is observed for the same input parameters of the disturbance. This representation method was applied for 9 simulations conducted for each type of imposed disturbance until they returned to the steady-state. These simulations were designed to encompass linear variations in both period and amplitude, encompassing the outcome's high range of values.

3.2 SHIFT'S CURVES DUE TO ROTATIONAL PULSE

3.2.1 UNIDIRECTIONAL

When substituting Eq. (7) with Eq. (6), changes in the behavior of the bow shock are observed at the stagnation line and exit domain, as depicted in Figure 14.a and Figure 14.b, respectively. The maximum shift in both regions occurs simultaneously when $\theta_{\text{max}} = 6°$ and $T = .04\ t_u$, while the minimum shift is observed when $\theta_{\text{max}} = 4°$ and $T = .04\ t_u$. Notably, $\Delta\xi$ exhibits an inverse relationship with T when $\theta_{\text{max}} = 6°$, displaying a nonlinear trend with an upward

concavity at $\theta_{\max} = 5°$ and a nonlinear trend with a downward concavity at $\theta_{\max} = 4°$. Conversely, $\Delta\xi$ demonstrates a direct proportionality to $\theta_{\max}$ when $T = .04$, displaying a nonlinear trend with an upward concavity at $T = .05$ and a direct proportionality at $T = .06$. The behavior is also observed at the exit of the domain but with a time-phase shift, greater intensity, and longer duration.

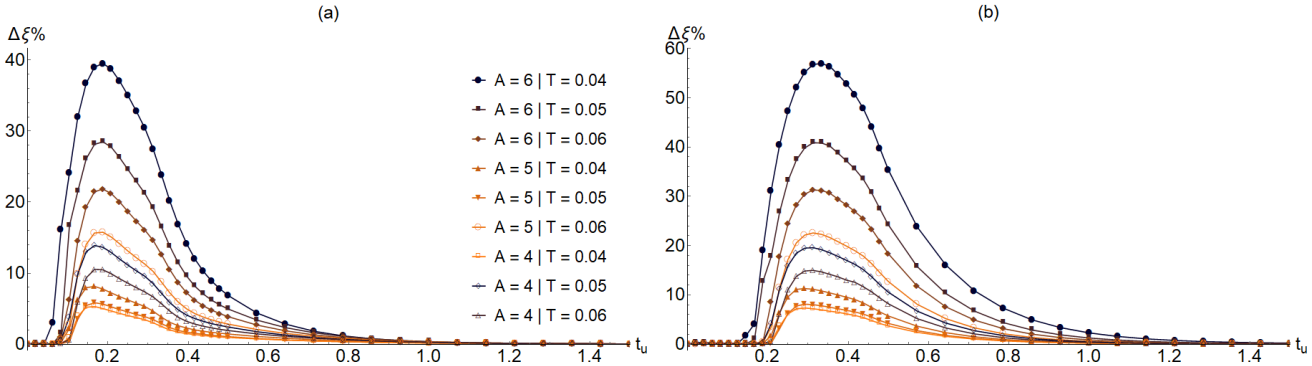

Figure 14. Shock position at the stagnation line (a) and at the exit domain (b), due to unidirectional angular stimuli.

3.2.2 BIDIRECTIONAL

Continues the analysis with Eq. (6), changes in the behavior of the bow shock are observed at the stagnation line and exit domain, as depicted in Fig. 15.a and Fig. 15.b, respectively. The maximum shift in both regions occurs simultaneously when $\theta_{\max} = 6°$ and $T = .04\ t_u$, but now the minimum shift is observed when $\theta_{\max} = 4°$ and $T = .06\ t_u$. Notably, $\Delta\xi$ exhibits an inverse relationship with T for all values of $\theta_{\max}$ presented. $\Delta\xi$ demonstrates a direct proportionality to $\theta_{\max}$ for all values of T too.

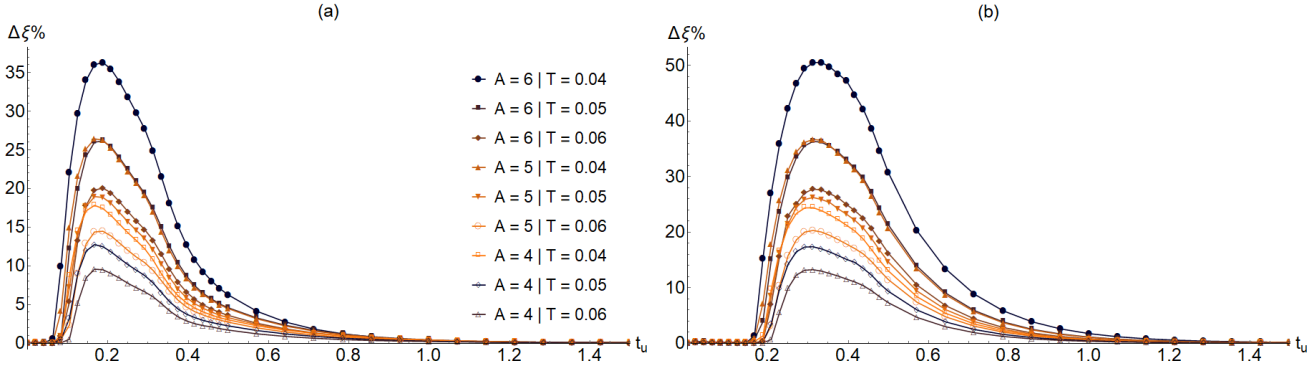

Figure 15. Shock position at the stagnation line (a) and at the exit domain (b), due to bidirectional angular stimuli.

3.3 SHIFT'S CURVES DUE TO NORMAL PULSE AT THE WALL

By setting the coefficient $\dot{\epsilon}_T$ to 0 in the Eq. (3) and performing the applicable Gaussian substitutions to θ_N, it becomes possible to introduce a normal pulse to the wall in the system. This yields a result similar to the excitement of a unitary dilating vibration in the cylinder, in which positive values lead to a contraction of all mesh points related to the cylinder wall towards the center and negative values cause the opposite.

3.3.1 UNIDIRETIONAL

At this time, the analysis with Eq. (6) culminates in the dislocations of the bow shock at the stagnation line and exit domain presented in Fig. 16.a and Fig. 16.b, respectively. The maximum shift in both regions occurs simultaneously when $\theta_{\max} = .04$ and $T = .05\ t_u$, and the minimum is observed when $\theta_{\max} = .02$ and $T = .06\ t_u$. Notably, $\Delta\xi$ exhibits an inverse relationship with T for $\theta_{\max}$ equals .02 and .03 and a nonlinear trend with a downward concavity for $\theta_{\max} = .04$. $\Delta\xi$ demonstrates nonlinearity with upward concavity for $\theta_{\max}$ for all values of T equals .04 and .05 but is directly proportional for $T = .06$.

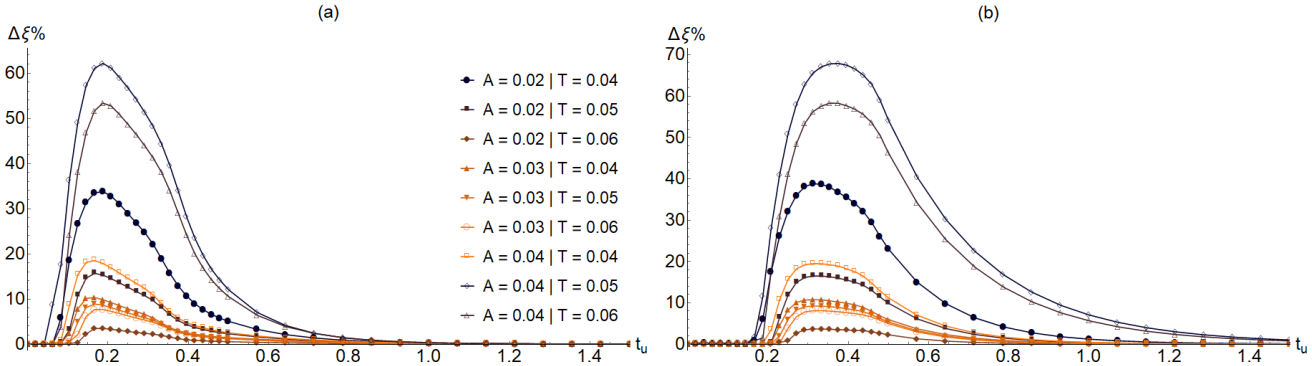

Figure 16. Shock position at the stagnation line (a) and at the exit domain (b), due to unidirectional dilatant stimuli.

3.3.2 BIDIRETIONAL

At this time, the analysis with Eq. (7) culminates in the dislocations of the bow shock at the stagnation line and exit domain presented in Fig. 17.a and Fig. 17.b, respectively. The maximum shift in both regions occurs simultaneously when $\theta_{\max} = .04$ and $T = .04\ t_u$, and the minimum is observed when $\theta_{\max} = .02$ and $T = .06\ t_u$. Notably, $\Delta\xi$ exhibits an inverse relationship with T for all values of $\theta_{\max}$. $\Delta\xi$ demonstrates inverse relationship with $\theta_{\max}$ for all values of T.

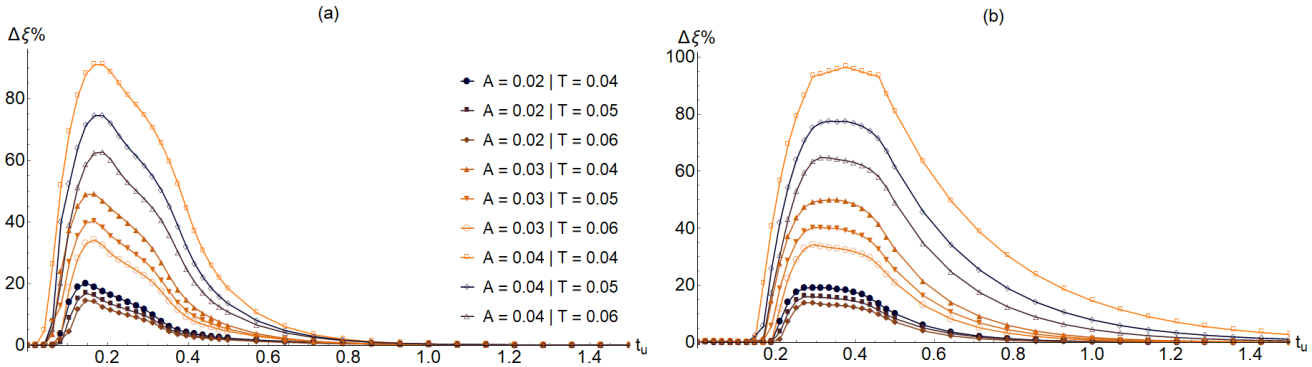

Figure 17. Shock position at the stagnation line (a) and at the exit domain (b), due to bidirectional dilatant stimuli.

4. CONCLUSION

The interaction between the pressure shock and the stationary shock results in an attenuation of the pressure propagated during the high-intensity stimulus and an upstream displacement of the bow shock in the same direction as the propagation. Additionally, the method applied in this work demonstrated an effective estimation of the shock line for stable shockwaves, i.e., those not being affected by stimuli from other parts of the flow, which in this article were chosen to originate from the cylinder wall.

The bow shock position can be estimated for numerous pressure curves in a two-dimensional mesh line bounded for the problem. However, the proposed method for parabolic shock extrapolation within the domain proved insufficient during the interaction with pulse stimuli due to the coexistence of two shapes in the shock. In this case, it would suffice to extrapolate data collection for more than 2 mesh directions η, at least one more next to the contact discontinuity of bow shock. After the full contact of the shock with the transient wave, the method proved to be satisfactory during their return to steady-state again.

Furthermore, the analysis of shock position shifts due to rotational and normal pulses in unidirectional and bidirectional scenarios provides valuable insights into the dynamic behavior of bow shock waves in a complex system. The study revealed distinct patterns in how these angular and dilatant stimuli affect the shock position at the stagnation line and exit domain. When introducing normal pulses to the wall, the behavior of the bow shock was similarly affected in unidirectional and bidirectional cases. The maximum shift occurred at specific parameter combinations, while the minimum shift was observed under different conditions.

In summary, this analysis highlights the intricate and non-linear interactions between angular and dilatant stimuli and their effects on shock position within the examined system. Understanding these patterns is crucial for predicting and controlling shock wave behavior in various practical applications. More robust studies are essential to determine the behavior of the shockwave under different conditions, as the results presented here indicate a variation in the outcomes based on the magnitude and period at which the transient stimulus was applied to the cylinder wall.

5. ACKNOWLEDGMENTS

The authors would like to express their profound gratitude to the Francisco Eduardo Mourão Saboya Postgraduate Program in Mechanical Engineering (PGMEC) at the Universidade Federal Fluminense (UFF) of Rio de Janeiro, Niteroi, Brazil, and its esteemed collaborators. Special appreciation is extended to Professor's Leonardo Santos de Brito Alves for his invaluable guidance and support throughout this research endeavor. Additionally, JCAS would like to thank FAPERJ for Mestrado Nota 10 scholarship.

6. REFERENCES

Abhyankar, S., Brown, J., Constantinescu, E.M., Ghosh, D., Smith, B.F. and Zhang, H., 2018. "Petsc/ts: A modern scalable ode/dae solver library". *arXiv preprint arXiv:1806.01437*.

Alves, L., 2021. "Instability free three-dimensional hypersonic laminar boundary-layer steady-states for linear and non-linear stability analyses". In *AFOSR/HVSI/ONR High-Speed Aerodynamics Annual Review Meeting*.

Anderson, John D., J., 2020. *Modern Compressible Flow With Historical Perspective*. McGraw-Hill, 4th edition. ISBN 978-1-260-57082-3.

Anderson, John D., J., 2023. *Hypersonic and High-Temperature Gas Dynamics*. American Institute of Aeronautics and Astronautics, 2nd edition. ISBN 978-1-56347-780-5.

Billig, F.S., 1967. "Shock-wave shapes around spherical- and cylindrical-nosed bodies". *Journal of Spacecraft and Rockets*, Vol. 4, No. 6, pp. 822–823.

Hirsch, C., 2007. *Numerical Computation of Internal and External Flows: Volume 1: Fundamentals of Computational Fluid Dynamics*. Elsevier, 2nd edition. ISBN 978-0-7506-6594-0.

Jiang, G.S. and Shu, C.W., 1996. "Efficient implementation of weighted eno schemes". *Journal of Computational Physics*.

Kundu, P.K. and Cohen, I.M., 2004. *Fluid Mechanics*. Elsevier, San Diego, California, 3rd edition.

Nunes, M.S.S., 2021. *Generation of Steady-States for Stationary and Convectively Unstable Flows Using the Frequency Displacement Procedure*. Master's thesis, Universidade Federal Fluminense, Niterói, Brazil. Pós-graduação em Engenharia Mecânica, Escola de Engenharia.

Santos, R.D. and Alves, L.S., 2019. "Generation of steady-states with discontinuities using minimal gain marching schemes". In *AIAA 2019*. American Institute of Aeronautics and Astronautics, Dallas, Texas. doi:10.2514/6.2019-2839.

Santos, R.D., 2020. *Um estudo sobre os métodos de Runge-Kutta com forte estabilidade linear e não linear*. Ph.d. dissertation, UFF - Universidade Federal Fluminense, Niterói.

7. RESPONSIBILITY NOTICE

The author Allan Rodrigo Souza, Leonardo Santos de Brito Alves, Juan Carlos Assis Silva and Rômulo Bessi Freitas are solely responsible for the printed material included in this paper.